

# Zero-Shot Self-Supervised Learning for MRI Reconstruction

Burhaneddin Yaman<sup>1,2</sup>

Seyed Amir Hossein Hosseini<sup>1,2</sup>

Mehmet Akçakaya<sup>1,2</sup>

<sup>1</sup> Department of Electrical and Computer Engineering, University of Minnesota, Minneapolis, MN, USA

<sup>2</sup> Center for Magnetic Resonance Research, University of Minnesota, Minneapolis, MN, USA

{yaman013, hosse049, akcakaya}@umn.edu

## Abstract

Deep learning (DL) has emerged as a powerful tool for accelerated MRI reconstruction, but these methods often necessitate a database of fully-sampled measurements for training. Recent self-supervised and unsupervised learning approaches enable training without fully-sampled data. However, a database of undersampled measurements may not be available in many scenarios, especially for scans involving contrast or recently developed translational acquisitions. Moreover, database-trained models may not generalize well when the unseen measurements differ in terms of sampling pattern, acceleration rate, SNR, image contrast, and anatomy. Such challenges necessitate a new methodology that can enable scan-specific DL MRI reconstruction without any external training datasets. In this work, we propose a zero-shot self-supervised learning approach to perform scan-specific accelerated MRI reconstruction to tackle these issues. The proposed approach splits available measurements for each scan into three disjoint sets. Two of these sets are used to enforce data consistency and define loss during training, while the last set is used to establish an early stopping criterion. In the presence of models pre-trained on a database with different image characteristics, we show that the proposed approach can be combined with transfer learning to further improve reconstruction quality.

## 1. Introduction

Magnetic resonance imaging (MRI) is a non-invasive, radiation-free medical imaging modality technique that provides excellent soft tissue contrast for diagnostic purposes. However, lengthy acquisition times in MRI remain a limitation. Accelerated MRI techniques acquire fewer measurements at a sub-Nyquist rate, and use redundancies in the acquisition system or the images to remove the resulting aliasing artifacts during reconstruction. In clinical MRI systems, multi-coil receivers are used during data acquisition. Parallel imaging (PI) is the most clinically used method for accelerated MRI, and exploits the redundancies between these coils for reconstruction [5, 18]. Compressed sensing (CS)

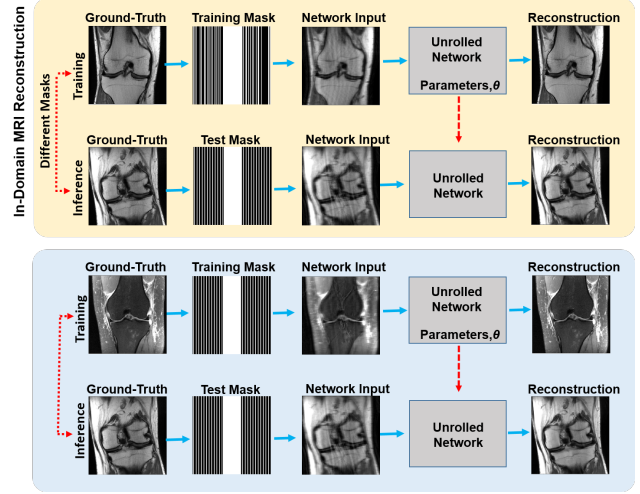


Figure 1. Test datasets may differ from the training datasets in terms of sampling pattern, SNR, contrast and anatomy. Such differences lead to suboptimal reconstructions in the test datasets, raising robustness and generalizability concerns for translation of trained models to clinical practice.

is another conventional accelerated MRI technique that exploits the compressibility of images in sparsifying transform domains [14], and is commonly used in combination with PI. However, PI and CS may suffer from noise and residual artifacts at high acceleration rates [19, 20].

Recently, deep learning (DL) methods have emerged as an alternative accelerated MRI technique due to their improved reconstruction quality compared to conventional approaches [6, 10]. Particularly, physics-guided deep learning reconstruction (PG-DLR) approaches have gained interest due to their robustness and improved reconstruction quality [1, 6, 8, 10, 21]. PG-DLR methods explicitly incorporate the physics of the data acquisition system into the neural network via a procedure known as algorithm unrolling [15]. This is done by unrolling conventional iterative algorithms that alternate between data consistency and regularization steps for a fixed number of iterations. Subsequently, PG-DLR approaches are trained in a supervised manner using large databases of fully-sampled measurements [1, 6]. More recently, self-supervised learning via data undersam-

pling (SSDU) has shown that similar reconstruction quality to supervised PG-DLR can be achieved while training on a database of only undersampled measurements [26].

While such database learning strategies offer improved reconstruction quality, acquisition of large datasets may not often be feasible. In some MRI applications involving time-varying physiological processes, dynamic information such as time courses of signal changes, contrast-related uptake or breathing patterns may differ substantially between subjects, making it difficult to generate high-quality databases of sufficient size for the aforementioned strategies. Furthermore, database training, in general, brings along concerns about generalization [3, 11]. In particular, measurement system parameters such as undersampling pattern or acceleration rates used in training may not match the unseen test dataset [9]. Moreover, the test data may have different imaging contrast, SNR, or anatomical features compared to the training database, which may lead to sub-optimal reconstruction [9, 16]. Finally, training datasets may lack examples of rare and/or subtle pathologies, increasing the risk of generalization failure [9, 11].

In this work, we tackle these challenges associated with database training, and propose zero-shot SSDU (ZS-SSDU), which performs scan-specific training of PG-DLR without any external training database. Succinctly, ZS-SSDU splits acquired measurements into three types of disjoint sets, which are respectively used only in the PG-DLR neural network, in defining the training loss, and in establishing a stopping strategy to avoid overfitting. In cases where a database-pretrained network is available, ZS-SSDU leverages transfer learning for improved reconstruction quality and reduced computational complexity.

Our contributions can be summarized as follows:

- We propose a zero-shot self-supervised method for learning MRI reconstruction from a single undersampled dataset without any external training database.
- We provide a well-defined methodology for determining stopping criterion to avoid over-fitting in contrast to other single-image training approaches [25].
- We synergistically combine the proposed zero-shot self-supervised learning approach with transfer learning (TL) to further reduce computational costs and achieve improved reconstruction quality.
- We apply the proposed zero-shot learning approach to knee and brain MRI datasets, and show its efficacy in removing residual aliasing and banding artifacts compared to supervised database learning.
- We show that the the proposed zero-shot learning in combination with TL may address robustness and generalizability issues of trained supervised models in terms of changes in sampling pattern, acceleration rate, contrast, SNR, and anatomy at inference time.

## 2. Background and Related Work

### 2.1. Accelerated MRI Acquisition Model

In MRI, raw measurement data is acquired in the frequency domain, also known as k-space. In current clinical MRI systems, multiple receiver coils are used, where each is sensitive to different parts of the volume. In practice, MRI is accelerated by taking fewer measurements, which are characterized by an undersampling mask denoting the acquired locations in k-space. For a multi-coil MRI acquisition, the forward model is given as

$$\mathbf{y}_i = \mathbf{P}_\Omega \mathcal{F} \mathbf{C}_i \mathbf{x} + \mathbf{n}_i, \quad i \in \{1, \dots, n_c\}, \quad (1)$$

where  $\mathbf{x}$  is the underlying image,  $\mathbf{y}_i$  are the acquired measurements for the  $i^{\text{th}}$  coil,  $\mathbf{P}_\Omega$  is the masking operator for undersampling pattern  $\Omega$ ,  $\mathcal{F}$  is the Fourier transform,  $\mathbf{C}_i$  is a diagonal matrix characterizing the sensitivity of the  $i^{\text{th}}$  coil,  $\mathbf{n}_i$  is measurement noise for  $i^{\text{th}}$  coil, and  $n_c$  is the number of coils [18]. This system is typically concatenated across the coil dimension to yield a compact representation

$$\mathbf{y}_\Omega = \mathbf{E}_\Omega \mathbf{x} + \mathbf{n}, \quad (2)$$

where  $\mathbf{y}_\Omega$  is the acquired undersampled measurements across all coils,  $\mathbf{E}_\Omega$  is the forward encoding operator that concatenates  $\mathbf{P}_\Omega \mathcal{F} \mathbf{C}_i$  across  $i \in \{1, \dots, n_c\}$ . The general inverse problem for accelerated MRI is given as

$$\arg \min_{\mathbf{x}} \|\mathbf{y}_\Omega - \mathbf{E}_\Omega \mathbf{x}\|_2^2 + \mathcal{R}(\mathbf{x}), \quad (3)$$

where the first term  $\|\mathbf{y}_\Omega - \mathbf{E}_\Omega \mathbf{x}\|_2^2$  enforces data consistency (DC) with acquired measurements and  $\mathcal{R}(\cdot)$  is a regularizer.

### 2.2. Parallel Imaging

The most clinically used acceleration strategy, PI uses linear methods to recover the image from the undersampled measurements  $\mathbf{y}_\Omega$ . PI performs reconstruction by solving Eq. 3 either without a regularizer term or with a Tikhonov regularizer [17]. The clinical implementation of PI relies on a so-called uniform undersampling pattern, where acquired k-space lines are equispaced. This leads to coherent foldover artifacts in the aliased images, but also allows a non-iterative unaliasing solution in the image domain [18]. We note that the problem can also be solved in k-space via interpolation [5]. PI typically suffers from noise amplification at high acceleration rates [5, 18].

### 2.3. Compressed Sensing

CS accelerates MRI acquisition by exploiting the compressibility of images in some transform domain, while requiring incoherent aliasing artifacts [14]. In CS reconstruction, a sparsity-inducing regularizer is used in Eq. 3. A popular choice is the  $\ell_1$  norm of transform-domain coefficients, in a fixed linear sparsifying domain, such as wavelets

[14]. CS-based approaches utilize random undersampling patterns to generate incoherent aliasing artifacts. One of the main limitations of CS approaches is blurring and residual artifacts seen at high acceleration rates [20].

## 2.4. PG-DLR with Algorithm Unrolling

Several optimization methods are available for solving the inverse problem in (3) [4]. Variable-splitting via quadratic penalty is one such approach that decouples the DC and regularizer units. It introduces an auxiliary variable  $\mathbf{z}$  that is constrained to be equal to  $\mathbf{x}$ , and (3) is reformulated as an unconstrained problem with a quadratic penalty

$$\arg \min_{\mathbf{x}, \mathbf{z}} \|\mathbf{y}_\Omega - \mathbf{E}_\Omega \mathbf{x}\|_2^2 + \mu \|\mathbf{x} - \mathbf{z}\|_2^2 + \mathcal{R}(\mathbf{z}), \quad (4)$$

where  $\mu$  is the penalty parameter. The optimization problem in Eq. (4) is then solved via alternating minimization as

$$\mathbf{z}^{(i)} = \arg \min_{\mathbf{z}} \mu \|\mathbf{x}^{(i-1)} - \mathbf{z}\|_2^2 + \mathcal{R}(\mathbf{z}), \quad (5a)$$

$$\mathbf{x}^{(i)} = \arg \min_{\mathbf{x}} \|\mathbf{y}_\Omega - \mathbf{E}_\Omega \mathbf{x}\|_2^2 + \mu \|\mathbf{x} - \mathbf{z}^{(i)}\|_2^2, \quad (5b)$$

where  $\mathbf{z}^{(i)}$  is an intermediate variable and  $\mathbf{x}^{(i)}$  is the desired image at iteration  $i$ . In PG-DLR, an iterative algorithm, as in (5a) and (5b) is unrolled for a fixed number of iterations [1, 6, 8, 13]. Each unrolled iteration contains a DC and a regularizer unit, in which the regularizer sub-problem in Eq. (5a) is implicitly solved with neural networks and the DC sub-problem in Eq. (5b) is solved via linear methods such as gradient descent [6] or conjugate gradient (CG) [1].

There have been numerous works on PG-DLR for accelerated MRI [1, 6, 13, 21, 26]. Most of these works vary from each other on the algorithms used for DC and neural networks employed in the regularizer units. However, all these works require a large database of training samples.

## 3. Methods

In this section, we review supervised and self-supervised PG-DLR training strategies. Subsequently, we introduce the proposed zero-shot self-supervised learning approach.

### 3.1. Supervised Learning for PG-DLR

In supervised PG-DLR, training is performed using a database of fully-sampled reference data. Let  $\mathbf{y}_{\text{ref}}^i$  be fully-sampled k-space for subject  $i$  and  $f(\mathbf{y}_\Omega^i, \mathbf{E}_\Omega^i; \theta)$  be the output of the unrolled network for under-sampled k-space  $\mathbf{y}_\Omega^i$ , where the network is parameterized by  $\theta$ . End-to-end training minimizes [10, 26]

$$\min_{\theta} \frac{1}{N} \sum_{i=1}^N \mathcal{L}(\mathbf{y}_{\text{ref}}^i, \mathbf{E}_{\text{full}}^i f(\mathbf{y}_\Omega^i, \mathbf{E}_\Omega^i; \theta)), \quad (6)$$

where  $N$  is the number of samples in the training database,  $\mathbf{E}_{\text{full}}^i$  is the fully-sampled encoding operator that transform network output to k-space and  $\mathcal{L}(\cdot, \cdot)$  is a loss function.

### 3.2. Self-Supervised Learning for PG-DLR

Unlike supervised learning, SSDU performs training without fully-sampled data by only utilizing acquired undersampled measurements [26]. In SSDU, the undersampled data indices,  $\Omega$  are split into two disjoint sets  $\Theta$  and  $\Lambda$  as  $\Omega = \Theta \cup \Lambda$ .  $\Theta$  is the set of k-space locations used in the DC units of the PG-DLR network during training, while  $\Lambda$  is a set of k-space locations used in the loss function. End-to-end training is performed using the loss function

$$\min_{\theta} \frac{1}{N} \sum_{i=1}^N \mathcal{L}(\mathbf{y}_\Lambda^i, \mathbf{E}_\Lambda^i (f(\mathbf{y}_\Theta^i, \mathbf{E}_\Theta^i; \theta))). \quad (7)$$

SSDU was also extended to a multi-mask setting [27], where  $\Omega$  is retrospectively split into disjoint sets  $\Theta_k$  and  $\Lambda_k$  multiple times. Hence, available measurements for each slice in the database are partitioned  $K$  times such that

$$\Omega = \Theta_k \cup \Lambda_k, \quad k \in \{1, \dots, K\}, \quad (8)$$

with  $\Lambda_k = \Omega \setminus \Theta_k$ , leading to the following training loss

$$\min_{\theta} \frac{1}{N \cdot K} \sum_{i=1}^N \sum_{k=1}^K \mathcal{L}(\mathbf{y}_{\Lambda_k}^i, \mathbf{E}_{\Lambda_k}^i (f(\mathbf{y}_{\Theta_k}^i, \mathbf{E}_{\Theta_k}^i; \theta))). \quad (9)$$

The multi-mask SSDU was shown to outperform the single-mask SSDU in terms of reconstruction quality [27].

### 3.3. Proposed Zero-Shot Learning for PG-DLR

The 2-way partitioning of data in Section 3.2 is reminiscent of cross-validation, where the available database is split into two sets, one of which is used to train the model and the other to test whether the trained model generalizes to unseen data. Similarly in SSDU, one set,  $\Theta$  is used within the network, while the other set,  $\Lambda$  is never seen by the network and is used to test the generalization performance to other k-space points by defining the loss. Note the main difference to cross-validation is that in SSDU, partitioning is performed for each slice in the training database, whereas cross-validation partitions the whole database only once.

While this 2-way partitioning can be applied for subject-specific learning, it leads to overfitting unless the training is stopped early [7]. This is similar to other single-image learning strategies, such as deep image prior (DIP) or zero-shot super-resolution [22, 25]. DIP-type approaches shows that an un-trained neural network can successfully perform instance-specific image restoration tasks such as denoising, super-resolution, inpainting without any training data. However, such DIP-type techniques requires an early stopping for avoiding over-fitting, which is typically done with a manual heuristic selection [7, 25]. Thus, in this work, we propose a zero-shot self-supervised learning via data undersampling (ZS-SSDU) approach for scan-specific PG-DLR with a well-defined automated early stopping criterion.

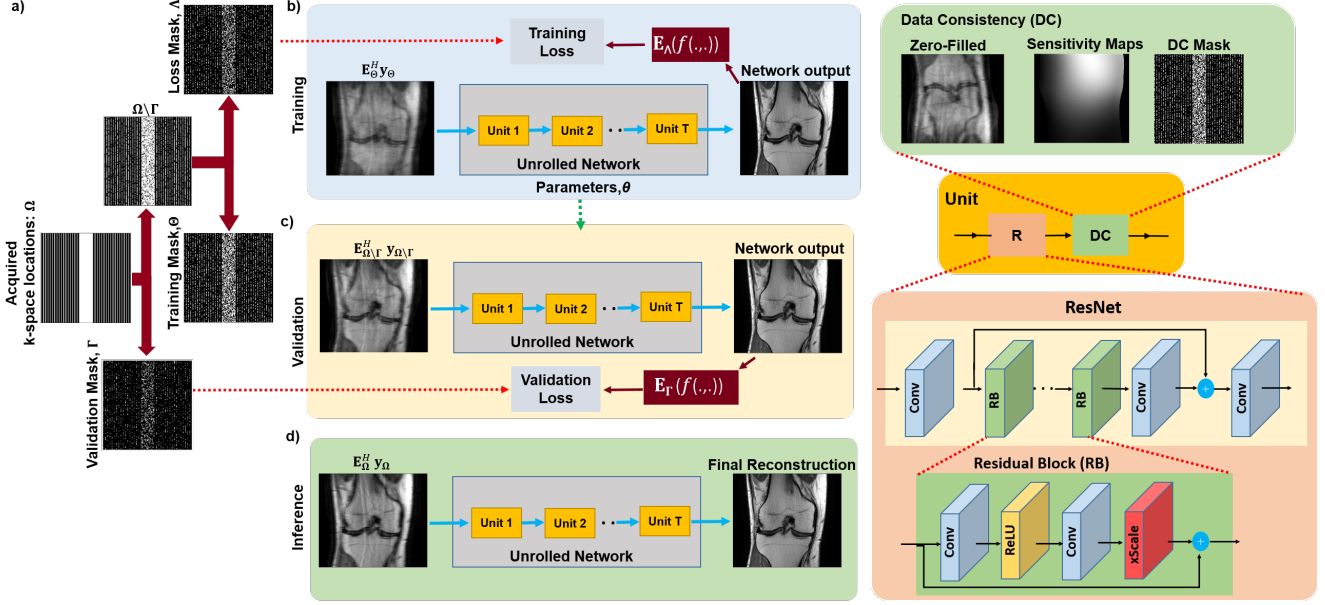


Figure 2. An overview of the proposed zero-shot self-supervised learning approach. a) Acquired measurements for the scan of interest are split into three sets: a training mask ( $\Theta$ ), a loss mask ( $\Lambda$ ), and a validation mask for automated early stopping ( $\Gamma$ ). b) The parameters,  $\theta$ , of the unrolled MRI reconstruction network are updated using  $\Theta$  and  $\Lambda$  in data consistency (DC) units of the unrolled network and for defining loss, respectively. c) Concurrently, a k-space validation procedure is used to establish the stopping criterion by using  $\Omega \setminus \Gamma$  in the DC units and  $\Gamma$  to measure a validation loss. d) Once the network training has been stopped due to an increasing trend in the validation loss, the final reconstruction is performed using the relevant learned network parameters and all the acquired measurements in the DC unit.

**ZS-SSDU Formulation and Training:** In this work, we extend the partitioning to a 3-way split, which is reminiscent of using a validation set in addition to testing and training sets for hyperparameter tuning and/or for regularization by early stopping. We define the following partition for  $\Omega$ :

$$\Omega = \Theta \sqcup \Lambda \sqcup \Gamma, \quad (10)$$

where  $\sqcup$  denotes a disjoint union, i.e.  $\Theta$ ,  $\Lambda$  and  $\Gamma$  are pairwise disjoint (Figure 2). Similar to Section 3.2,  $\Theta$  is used in the DC units of the unrolled network, and  $\Lambda$  is used to define the loss in k-space. The third partition  $\Gamma$  is a set of acquired k-space indices that are set aside for defining a k-space validation loss.

ZS-SSDU can be formulated in the multi-mask setting [27], by fixing the k-space validation partition  $\Gamma \subset \Omega$ , and performing the multi-masking on  $\Omega \setminus \Gamma$ . Formally,  $\Omega \setminus \Gamma$  is partitioned  $K$  times such that

$$\Omega \setminus \Gamma = \Theta_k \sqcup \Lambda_k, \quad k \in \{1, \dots, K\}, \quad (11)$$

where  $\Lambda_k$ ,  $\Theta_k$  and  $\Gamma$  are pairwise disjoint, i.e.  $\Omega = \Gamma \sqcup \Theta_k \sqcup \Lambda_k, \forall k$ . Thus, ZS-SSDU performs training by minimizing

$$\min_{\theta} \frac{1}{K} \sum_{k=1}^K \mathcal{L}(\mathbf{y}_{\Lambda_k}, \mathbf{E}_{\Lambda_k}(f(\mathbf{y}_{\Theta_k}, \mathbf{E}_{\Theta_k}; \theta)))$$

This is now supplemented by a new k-space validation loss, which tests the generalization performance of the trained

network on the k-space validation partition  $\Gamma$ . For the  $l^{\text{th}}$  epoch, where the learned network weights are specified by  $\theta^{(l)}$ , this validation loss is given by:

$$\mathcal{L}(\mathbf{y}_{\Gamma}, \mathbf{E}_{\Gamma}(f(\mathbf{y}_{\Omega \setminus \Gamma}, \mathbf{E}_{\Omega \setminus \Gamma}; \theta^{(l)}))). \quad (12)$$

Note that in (12), the network output is calculated by applying the DC units on  $\Omega \setminus \Gamma = \Theta \sqcup \Lambda$ , i.e. all acquired points outside of  $\Gamma$ , to better assess its generalizability performance. The key idea is that while the training loss will decrease over epochs, the k-space validation loss will start increasing once overfitting is observed. Thus, we monitor the loss in (12) during training to define an early stopping criterion to avoid overfitting. Let  $L$  be the epoch in which training needs to be stopped. Then at inference time, the network output is calculated as  $f(\mathbf{y}_{\Omega}, \mathbf{E}_{\Omega}; \theta^{(L)})$ , i.e. all acquired points are used to calculate the network output [26].

**ZS-SSDU with Transfer Learning (TL):** TL has been used for re-training DL models pre-trained on large databases to reconstruct MRI data with different characteristics [9]. However, such transfer still requires another, often smaller database for re-training. In contrast, in the presence of pre-trained models, ZS-SSDU can be combined with TL, referred to as ZS-SSDU-TL, to reconstruct a single dataset with different characteristics by using weights of the pre-trained model for initialization. This facilitates faster convergence, reducing the reconstruction time.



## 4. Experiments

### 4.1. Datasets

We performed experiments on publicly available fully-sampled multi-coil knee and brain MRI from fastMRI database [12]. Knee and brain MRI datasets contained data from 15 and 16 receiver coils, respectively. Fully-sampled datasets were retrospectively undersampled by keeping 24 lines of autocalibrated signal (ACS) from center of k-space. FastMRI database contains different contrast weightings. For knee MRI, we used coronal proton density (Cor-PD) and coronal proton density with fat suppression (Cor-PDFS) and for brain MRI, axial Flair(Ax-FLAIR) and axial T2 (Ax-T2). Figure 3 shows the different datasets used in this study, as well as different types of undersampling masks.

### 4.2. Implementation Details

All PG-DLR approaches were trained end-to-end using 10 unrolled iterations. CG method and a ResNet structure were employed in the DC and regularizer units of the unrolled network, respectively [26]. ResNet is comprised of a layer of input and output convolution layers, and 15 residual blocks (RB) each containing two convolutional layers, where the first layer is followed by ReLU and the second layer is followed by a constant multiplication [23]. All layers had a kernel size of  $3 \times 3$ , 64 channels. The real and imaginary parts of the complex MR images were concatenated prior to being input to the ResNet as 2-channel images. The unrolled network, which shares parameters across the unrolled iterations had a total of 592,129 trainable parameters. Coil sensitivity maps were generated from the central  $24 \times 24$  ACS using ESPIRiT [24]. End-to-end training was performed with a normalized  $\ell_1$ - $\ell_2$  loss (Adam optimizer,  $LR=5 \cdot 10^{-4}$ , batch size=1) [26]. Peak signal-to-

noise ratio (PSNR) and structural similarity index (SSIM) were used as quantitative evaluation criteria.

### 4.3. Reconstruction Method Comparisons

In this work, we focus on comparing training strategies for accelerated MRI reconstruction. Thus, we used the same network architecture from Section 4.2 for all training methods in all experiments. We note that the proposed ZS-SSDU training strategy is agnostic to the specifics of the neural network architecture, and the neural network for the regularizer unit [23] was not tuned in any way. In fact, the number of tunable network parameters is higher than the number of undersampled measurements available on a single dataset, i.e. dimension of  $y_\Omega$ . As such, different neural network architectures may be used for the regularizer unit in the unrolled network, but this is not the focus of our study.

**Supervised PG-DLR:** Supervised PG-DLR models for knee and brain MRI were trained on 300 slices from 15 and 30 different subjects, respectively. For each knee and brain contrast weighting, two networks were trained separately using random and uniform masks [6] at an acceleration rate (R) of 4 [11]. Trained networks were used for comparison and TL purposes. We note that random undersampling results in incoherent artifacts, whereas uniform undersampling leads to coherent artifacts that are harder to remove (Figure 3) [9]. Hence, we focus on the more difficult problem of uniform undersampling, while presenting random undersampling results in Supplementary Materials.

**DIP-Recon:** We employ a DIP-type scan-specific MRI reconstruction that uses all acquired measurements in both DC and defining loss [26]:

$$\mathcal{L}(y_\Omega, E_\Omega(f(y_\Omega, E_\Omega; \theta))). \quad (13)$$

We refer to the reconstruction from this training mechanism as DIP-Recon. DIP-Recon-TL refers to combining (13) with TL. As mentioned, DIP-Recon does not have a stopping criterion, hence early stopping was heuristically determined (Supplementary Figure S1).

**Parallel Imaging:** We include CG-SENSE, which is a commonly used scan-specific conventional PI method [17, 18], as the clinical baseline quality for comparison purposes.

### 4.4. Automated Stopping and Ablation Study

The stopping criterion for the proposed ZS-SSDU was investigated on slices from the knee dataset. Validation set  $\Gamma$  was selected from the acquired measurements  $\Omega$  using a uniformly random selection with  $|\Gamma|/|\Omega| = 0.2$ . The remaining acquired measurements  $\Omega \setminus \Gamma$  were retrospectively split into disjoint 2-tuples multiple times based on uniformly random selection with the ratio  $\rho = |\Lambda_k|/|\Omega \setminus \Gamma| = 0.4 \forall k \in \{1, \dots, K\}$  [26].

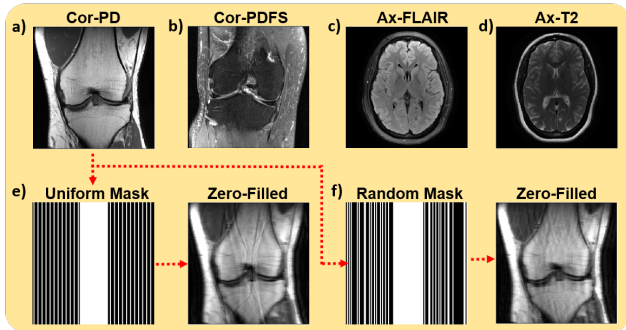


Figure 3. Different contrast weightings and anatomies: a) Cor-PD, b) Cor-PDFS, c) Ax-FLAIR, d) Ax-T2, as well as undersampling patterns: e) Uniform, f) Random mask, used in this study. Zero-filled images generated by uniform and random undersampling masks have coherent and incoherent aliasing artifacts, respectively. Coherent aliasing artifacts are generally harder to remove compared to incoherent artifacts.

Figure 4a shows representative scan-specific training and validation loss curves at  $R = 4$  of ZS-SSDU for  $K \in \{1, 10, 25, 50\}$ . As expected, training loss decreases with increasing epochs for all  $K$ . Validation loss for  $K = 1$  decreases without showing a clear breaking point for stopping. For  $K > 1$ , validation loss forms an L-curve, and the breaking point of the L-curve is used as the stopping criterion. Figure 4b shows reconstructions corresponding to the  $K$  values using the proposed stopping criterion. For  $K > 1$ , no visible residual aliasing artifacts are observed. For  $K = 1$ , without a clear breaking point for stopping criterion, reconstructions show lower visual and quantitative quality.  $K = 10$  is used for the rest of the study, while noting  $K = 25$  and  $50$  also show similar performance.

Figure 5a and b show loss curves and reconstruction results on a Cor-PD slice with and without transfer learning. ZS-SSDU-TL, which uses pre-trained supervised PG-DLR parameters as initial starting parameters, converges faster compared to ZS-SSDU, substantially reducing the total training time. Both ZS-SSDU and ZS-SSDU-TL remove residual artifacts, while the latter shows visually and quantitatively improved reconstruction performance.

#### 4.5. Reconstruction Results

In the first set of experiments, we compare all the methods when the testing and training data belongs to the same knee or brain MRI contrast weighting with the same acceleration rate and undersampling mask. These experiments aim to show the efficacy of the proposed approach in performing scan-specific MRI reconstruction, while removing residual aliasing artifacts. We also note that this is the most

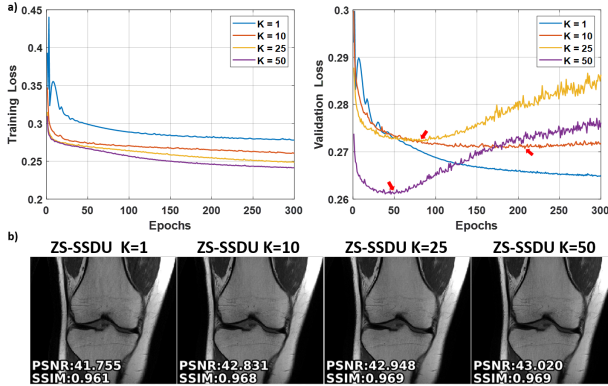


Figure 4. a) Representative training and k-space validation loss curves for ZS-SSDU with multiple  $K \in \{1, 10, 25, 50\}$  masks on Cor-PD knee MRI using uniform undersampling at  $R = 4$ . For  $K > 1$  the validation loss forms an L-curve, whose breaking point (red arrows) dictates the automated early stopping criterion for training. b) Corresponding ZS-SSDU reconstruction results. At  $K = 1$ , without a clear stopping criterion, visible artifacts remain, highlighting the overfitting. For  $K > 1$ , ZS-SSDU shows good reconstruction quality without residual artifacts.

favorable setup for database-trained supervised PG-DLR.

In the subsequent experiments, we focus on the reported generalization and robustness issues with database-trained PG-DLR methods [2, 9, 11, 16]. We investigate banding artifacts, as well as in-domain and cross-domain transfer cases. For these experiments, we concentrate on ZS-SSDU-TL, since ZS-SSDU has no prior domain information, and is inherently not susceptible to such generalizability issues.

**Comparison of Reconstruction Methods:** In these experiments, supervised PG-DLR was trained and tested using uniform undersampling at  $R = 4$ , representing a perfect match for training and testing conditions. Figure 6a and b show reconstruction results for Cor-PD knee and Ax-FLAIR brain MRI datasets in this setting. CG-SENSE reconstruction suffers from significant residual artifacts and noise amplification in Cor-PD knee and Ax-FLAIR brain MRIs, respectively. Similarly, both DIP-Recon and DIP-Recon-TL suffer from residual artifacts and noise amplification. Supervised PG-DLR achieves artifact-free reconstruction. Both ZS-SSDU and ZS-SSDU-TL also perform artifact-free reconstruction with similar image quality. Table 1 shows the average SSIM and PSNR values on 30 test slices. Similar observations apply when random undersampling employed (Supplementary Figure S2). While supervised PG-DLR generally works well when the training and test data characteristics are matched, it may still suffer from residual artifacts in some cases, which are successfully suppressed by ZS-SSDU methods (Supplementary Figure S3).

**Banding Artifacts:** Banding artifacts appear in the form of streaking horizontal lines, and occur due to high acceleration rates and anisotropic sampling [2]. These hinder radiological evaluation and are regarded as a barrier for the translation of DL reconstruction methods into clinical prac-

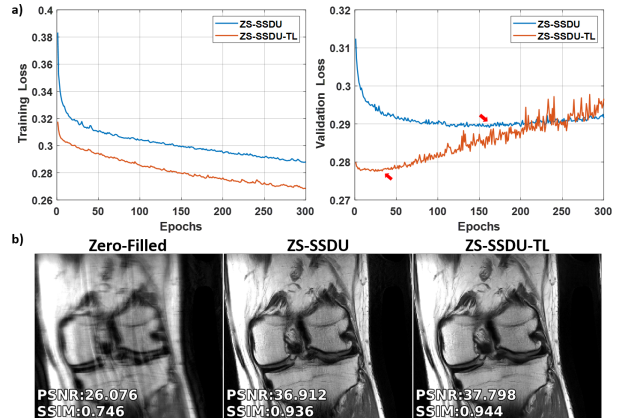


Figure 5. a) Loss curves for ZS-SSDU with/without TL for  $K = 10$  on a representative Cor-PD knee MRI slice. ZS-SSDU with TL converges faster compared to ZS-SSDU (red arrows). b) Reconstruction results corresponding to the loss curves. Both ZS-SSDU and ZS-SSDU-TL remove residual artifacts.

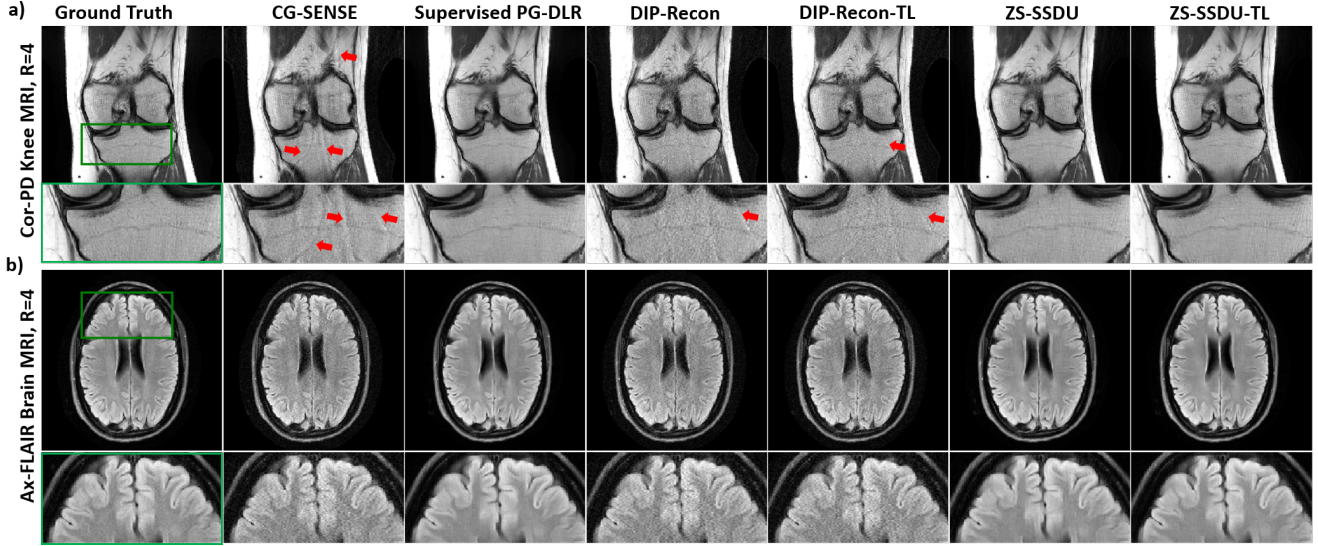


Figure 6. Reconstruction results on a representative test slice from a) Cor-PD knee MRI and b) Ax-FLAIR brain MRI at  $R = 4$  with uniform undersampling. CG-SENSE, DIP-Recon, DIP-Recon-TL suffer from noise amplification and residual artifacts shown with red arrows, especially in knee MRI due to the unfavorable coil geometry. Scan-specific ZS-SSDU and ZS-SSDU-TL achieve artifact-free and improved reconstruction quality, similar to the database-trained supervised PG-DLR.

time [2]. This set of experiments explored training and testing on Cor-PDFS data, where database-trained PG-DLR reconstruction has been reported to show such artifacts [2, 16]. Figure 7 shows reconstructions for a Cor-PDFS test slice. While DIP-Recon-TL suffers from clearly visible noise amplification, supervised PG-DLR suffers from banding artifacts shown with yellow arrows. ZS-SSDU-TL significantly alleviates these banding artifacts in the reconstruction. While supervised PG-DLR achieves slightly better SSIM and PSNR (Supplementary Table S1), we note that banding artifacts do not necessarily correlate with such metrics, and are usually picked up in expert readings [2, 11].

**In-Domain Transfer:** In these experiments, we compared the in-domain generalizability of database-trained PG-DLR and scan-specific PG-DLR. For in-domain transfer, training and test datasets are of the same type of data, but may differ from each other in terms of acceleration and undersampling pattern (Figure 1). In Figure 8a, supervised PG-DLR was trained with random undersampling and tested on uniform undersampling. Supervised PG-DLR fails to generalize and suffers from residual aliasing artifacts (red arrows), consistent with previous reports [9, 16]. Similarly, DIP-Recon-TL suffers from artifacts and noise amplification. Proposed ZS-SSDU-TL achieves an artifact-free and

improved reconstruction quality. In Figure 8b, supervised PG-DLR was trained with uniform undersampling at  $R = 4$  and tested on uniform undersampling at  $R = 6$ . While both supervised PG-DLR and DIP-Recon-TL suffers from aliasing artifacts, ZS-SSDU-TL successfully removes these artifacts. Average PSNR and SSIM values align with the observations (Supplementary Table S1).

**Cross-Domain Transfer:** In the last set of experiments, we investigated the cross-domain generalizability of database-trained PG-DLR compared to scan-specific trained PG-DLR. For cross-domain transfer, training and test datasets are of the different data characteristics and generally differ in terms of contrast, SNR, and anatomy (Figure 1). In Figure 9, supervised PG-DLR was trained on Cor-PDFS and Ax-T2 at  $R = 4$  with uniform sampling, but tested on Cor-PD and Ax-FLAIR at  $R = 4$  with uniform undersampling, respectively. In both cases, supervised PG-DLR fails to generalize and has residual artifacts (red arrows). Similarly, DIP-Recon-TL suffers from artifacts and noise. ZS-SSDU-TL achieves an artifact-free improved reconstruction.

Figure 10 shows the performance when the testing anatomy differs from training anatomy. Supervised PG-DLR was trained on Cor-PD and Ax-FLAIR at  $R = 4$  with uniform sampling, and tested on Ax-FLAIR and Cor-PD

	Metrics	CG-SENSE	Supervised PG-DLR	DIP-Recon	DIP-Recon-TL	ZS-SSDU	ZS-SSDU-TL
Cor-PD	SSIM	0.862	<b>0.952</b>	0.793	0.819	0.948	0.951
	PSNR	34.521	39.966	32.668	33.583	39.550	<b>40.102</b>
Ax-FLAIR	SSIM	0.836	0.934	0.799	0.818	0.935	<b>0.937</b>
	PSNR	31.969	<b>37.375</b>	30.637	31.249	36.861	37.250

Table 1. Average PSNR and SSIM values on 30 test slices.



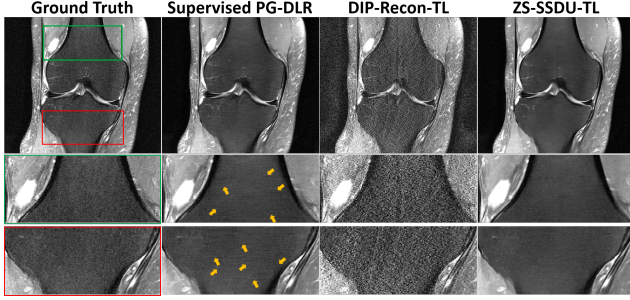


Figure 7. Supervised PG-DLR suffers from banding artifacts (yellow arrows), while ZS-SSDU-TL significantly alleviates these artifacts. DIP-Recon-TL suffers from clear noise amplification.

at  $R=4$  with uniform undersampling, respectively. In both cases, supervised PG-DLR fails to generalize across different anatomies with visible residual artifacts. DIP-Recon-TL also suffers from artifacts and noise amplification in Cor-PD and Ax-FLAIR, respectively. ZS-SSDU-TL successfully removes noise and residual artifacts. For both cross-domain transfer experiments, average PSNR and SSIM values match our observations (Supplementary Table S1).

## 5. Conclusions

We proposed a self-supervised zero-shot deep learning method, ZS-SSDU, for scan-specific accelerated MRI reconstruction from a single undersampled dataset. The main ideas in ZS-SSDU were to divide the acquired measurement data into three types of disjoint sets, and use these in the PG-DLR network, for training loss, and for an automated early stopping criterion to avoid overfitting. In particular, we showed that with our training methodology and automated stopping criterion, scan-specific zero-shot learning of PG-DLR can be achieved *even when the number of tunable network parameters is higher than the number of available*

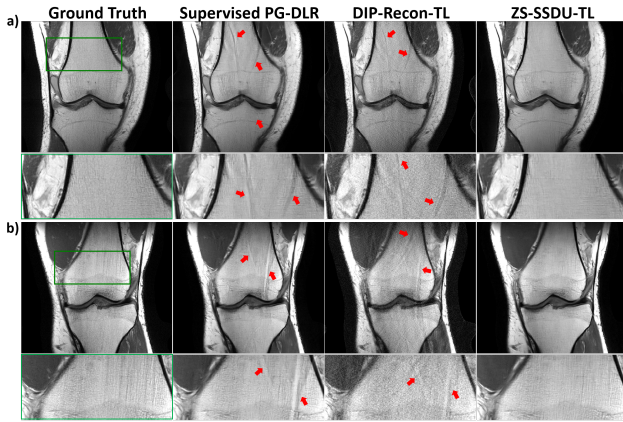


Figure 8. Supervised PG-DLR was trained with a) random mask and tested on uniform mask, both at  $R = 4$ ; b) uniform mask at  $R = 4$  and tested on uniform mask at  $R = 6$ . In both cases, supervised PG-DLR and DIP-Recon-TL suffer from visible artifacts (red arrows). ZS-SSDU-TL achieves artifact-free reconstruction.

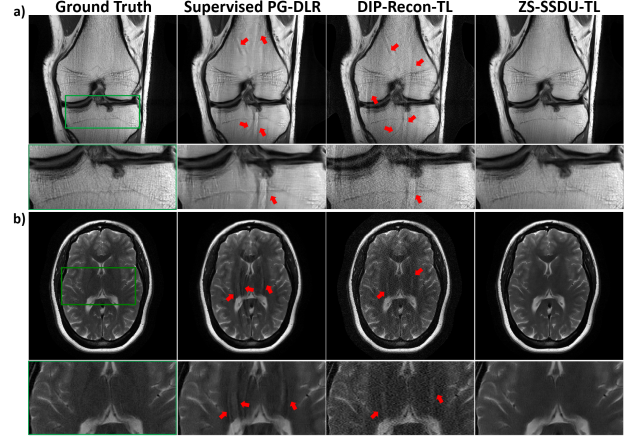


Figure 9. Using pre-trained a) Cor-PDFs and b) Ax-FLAIR models for Cor-PD and Ax-T2 reconstructions, respectively. Supervised PG-DLR fails to generalize when contrast and SNR changes, with residual artifacts (red arrows). DIP-Recon-TL also shows artifacts. ZS-SSDU-TL successfully removes noise and artifacts.

*measurements*. Our training method is not dependent on the particulars of the PG-DLR network architectures, and may be applied to different networks [1, 6, 13, 21, 26]. Finally, we also combined ZS-SSDU with transfer learning, in cases where a pre-trained model may be available, to further reduce reconstruction time and improve performance. Our results showed that ZS-SSDU methods perform similarly to database-trained supervised PG-DLR when training and testing data are matched, and they significantly outperform database-trained methods in terms of artifact reduction and generalizability when the training and testing data differ in terms of image characteristics and acquisition parameters.

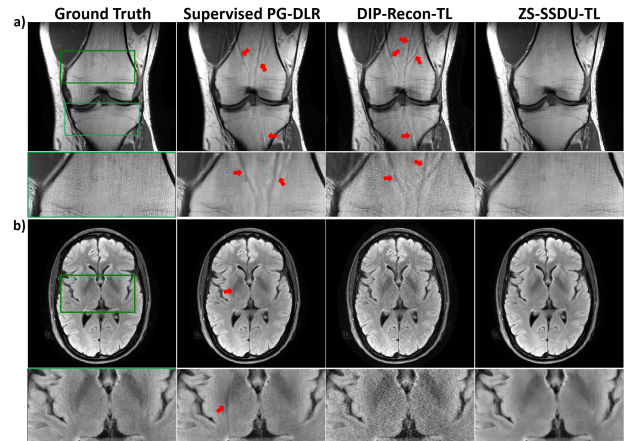


Figure 10. Using pre-trained a) Ax-FLAIR and b) Cor-PD models for Cor-PD and Ax-FLAIR reconstructions, respectively. When used across different anatomies, supervised PG-DLR exhibits artifacts (red arrows). While DIP-Recon-TL also has artifacts, ZS-SSDU-TL achieves artifact-free reconstruction in both cases.



## References

- [1] H. K. Aggarwal, M. P. Mani, and M. Jacob. MoDL: Model-based deep learning architecture for inverse problems. *IEEE Trans Med Imaging*, 38:394–405, 2019. 1, 3, 8
- [2] A. Defazio, T. Murrell, and M. Recht. MRI banding removal via adversarial training. In *Advances in Neural Information Processing Systems*, volume 33, pages 7660–7670. Curran Associates, Inc., 2020. 6, 7
- [3] Y. C. Eldar, A. O. Hero III, L. Deng, J. Fessler, J. Kovacevic, H. V. Poor, and S. Young. Challenges and open problems in signal processing: Panel discussion summary from ICASSP 2017. *IEEE Signal Processing Magazine*, 34:8–23, 2017. 2
- [4] J. A. Fessler. Optimization methods for magnetic resonance image reconstruction: Key models and optimization algorithms. *IEEE Signal Processing Magazine*, 37(1):33–40, 2020. 3
- [5] M. A. Griswold, P. M. Jakob, R. M. Heidemann, M. Nittka, V. Jellus, J. Wang, B. Kiefer, and A. Haase. Generalized autocalibrating partially parallel acquisitions (GRAPPA). *Magn Reson Med*, 47:1202–1210, 2002. 1, 2
- [6] K. Hammernik, T. Klatzer, E. Kobler, M. P. Recht, D. K. Sodickson, T. Pock, and F. Knoll. Learning a variational network for reconstruction of accelerated MRI data. *Magn Reson Med*, 79:3055–3071, 2018. 1, 3, 5, 8
- [7] S. A. H. Hosseini, B. Yaman, S. Moeller, and M. Akçakaya. High-fidelity accelerated MRI reconstruction by scan-specific fine-tuning of physics-based neural networks. In *IEEE Engineering in Medicine Biology Society (EMBC)*, pages 1481–1484, 2020. 3
- [8] S. A. H. Hosseini, B. Yaman, S. Moeller, M. Hong, and M. Akçakaya. Dense recurrent neural networks for accelerated MRI: History-cognizant unrolling of optimization algorithms. *IEEE J. Sel. Top. Signal Process.*, 14(6):1280–1291, 2020. 1, 3
- [9] F. Knoll, K. Hammernik, E. Kobler, T. Pock, M. P. Recht, and D. K. Sodickson. Assessment of the generalization of learned image reconstruction and the potential for transfer learning. *Magn Reson Med*, 81(1):116–128, 01 2019. 2, 4, 5, 6, 7
- [10] F. Knoll, K. Hammernik, C. Zhang, S. Moeller, T. Pock, D. K. Sodickson, and M. Akçakaya. Deep-learning methods for parallel magnetic resonance imaging reconstruction. *IEEE Signal Processing Magazine*, 37(1):128–140, 2020. 1, 3
- [11] F. Knoll, T. Murrell, et al. Advancing machine learning for MR image reconstruction with an open competition: Overview of the 2019 fastMRI challenge. *Magn Reson Med*, Jun 2020. 2, 5, 6, 7
- [12] F. Knoll, J. Zbontar, et al. fastMRI: A publicly available raw k-space and DICOM dataset of knee images for accelerated MR image reconstruction using machine learning. *Radiology AI*, page e190007, 2020. 5
- [13] D. Liang, J. Cheng, Z. Ke, and L. Ying. Deep magnetic resonance image reconstruction: Inverse problems meet neural networks. *IEEE Sig Proc Mag*, 37(1):141–151, 2020. 3, 8
- [14] M. Lustig, D. Donoho, and J. Pauly. Sparse MRI: The application of compressed sensing for rapid MR imaging. *Magn Reson Med*, 58:1182–1195, 2007. 1, 2, 3
- [15] V. Monga, Y. Li, and Y. C. Eldar. Algorithm unrolling: Interpretable, efficient deep learning for signal and image processing. *IEEE Signal Processing Magazine*, 38(2):18–44, 2021. 1
- [16] M. J. Muckley, B. Riemenschneider, et al. State-of-the-art machine learning mri reconstruction in 2020: Results of the second fastmri challenge. *arXiv preprint arXiv:2012.06318*, 2020. 2, 6, 7
- [17] K. P. Pruessmann, M. Weiger, P. Bornert, and P. Boesiger. Advances in sensitivity encoding with arbitrary k-space trajectories. *Magn Reson Med*, 46:638–651, 2001. 2, 5
- [18] K. P. Pruessmann, M. Weiger, M. B. Scheidegger, and P. Boesiger. SENSE: Sensitivity encoding for fast MRI. *Magn Reson Med*, 42:952–962, 1999. 1, 2, 5
- [19] P. M. Robson, A. K. Grant, A. J. Madhuranthakam, R. Lattanzi, D. K. Sodickson, and C. A. McKenzie. Comprehensive quantification of signal-to-noise ratio and g-factor for image-based and k-space-based parallel imaging reconstructions. *Magn Reson Med*, 60(4):895–907, Oct 2008. 1
- [20] C. M. Sandino, J. Y. Cheng, F. Chen, M. Mardani, J. M. Pauly, and S. S. Vasanawala. Compressed sensing: From research to clinical practice with deep neural networks: Shortening scan times for magnetic resonance imaging. *IEEE Signal Processing Magazine*, 37(1):117–127, 2020. 1, 3
- [21] J. Schlemper, J. Caballero, J. V. Hajnal, A. N. Price, and D. Rueckert. A deep cascade of convolutional neural networks for dynamic MR image reconstruction. *IEEE Trans Med Imaging*, 37:491–503, 2018. 1, 3, 8
- [22] A. Shocher, N. Cohen, and M. Irani. “Zero-shot” super-resolution using deep internal learning. In *Proc IEEE CVPR*, June 2018. 3
- [23] R. Timofte, E. Agustsson, L. Van Gool, M. H. Yang, and L. Zhang. NTIRE 2017 challenge on single image super-resolution: Methods and results. In *Proc IEEE CVPR*, 2017. 5
- [24] M. Uecker, P. Lai, M. J. Murphy, P. Virtue, M. Elad, J. M. Pauly, S. S. Vasanawala, and M. Lustig. ESPIRiT—an eigenvalue approach to autocalibrating parallel MRI: where SENSE meets GRAPPA. *Magn Reson Med*, 71(3):990–1001, Mar 2014. 5
- [25] D. Ulyanov, A. Vedaldi, and V. Lempitsky. Deep image prior. In *Proc. IEEE CVPR*, June 2018. 2, 3
- [26] B. Yaman, S. A. H. Hosseini, S. Moeller, J. Ellermann, K. Ugurbil, and M. Akçakaya. Self-supervised learning of physics-guided reconstruction neural networks without fully-sampled reference data. *Magn Reson Med*, 84:3172–3191, Dec 2020. 2, 3, 4, 5, 8
- [27] B. Yaman, S. A. H. Hosseini, S. Moeller, J. Ellermann, K. Ugurbil, and M. Akçakaya. Multi-mask self-supervised learning for physics-guided neural networks in highly accelerated MRI. *arXiv preprint arXiv:2008.06029*, 2020. 3, 4

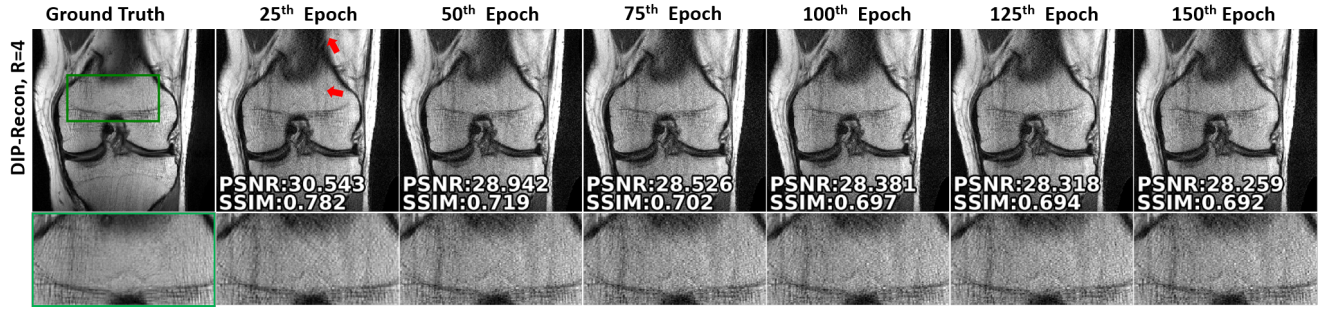


Figure S1. Cor-PD Knee MRI reconstruction results across different epochs for DIP-Recon using uniform undersampling at  $R = 4$ . At the 25th epoch, the reconstruction suffers from artifacts, with the zoom-in area showing texture that does not resemble the ground truth. With more epochs, this aspect of the reconstruction improves, but the reconstruction starts to suffer from noise amplification as the number of epochs increases. Hence, the 50th epoch was used in the experiments.

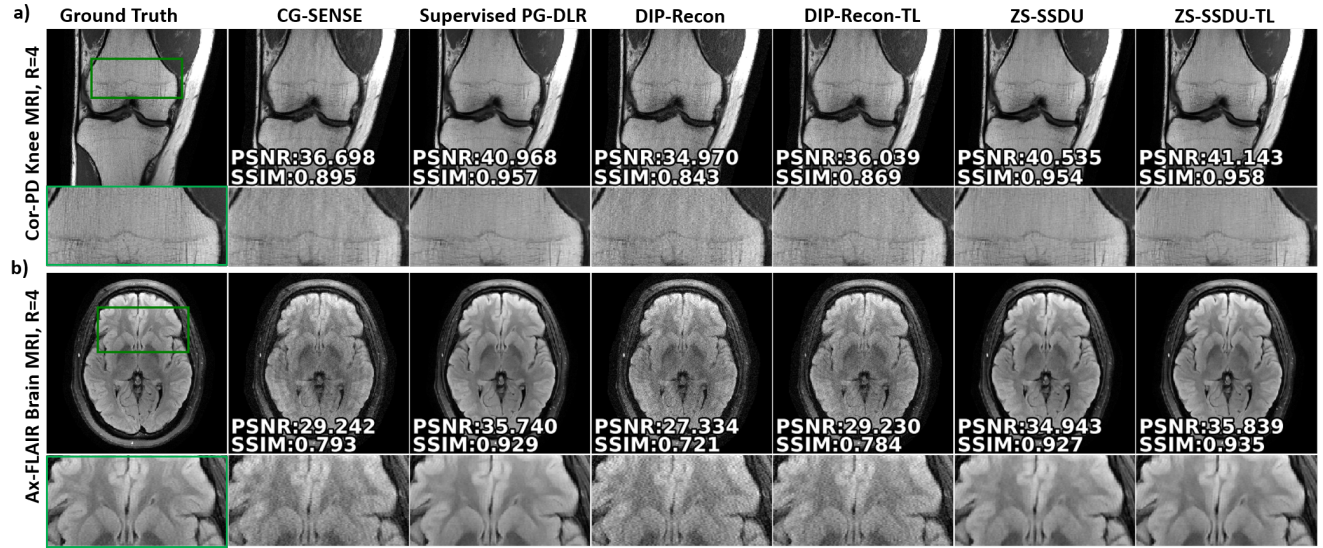


Figure S2. Reconstruction results from  $R = 4$  with random undersampling on representative test slices from a) Cor-PD knee MRI and b) Ax-FLAIR brain MRI. CG-SENSE, DIP-Recon and DIP-Recon-TL suffer from noise amplification. Supervised PG-DLR, ZS-SSDU and ZS-SSDU-TL all show artifact-free reconstruction quality, with similar quantitative metrics.

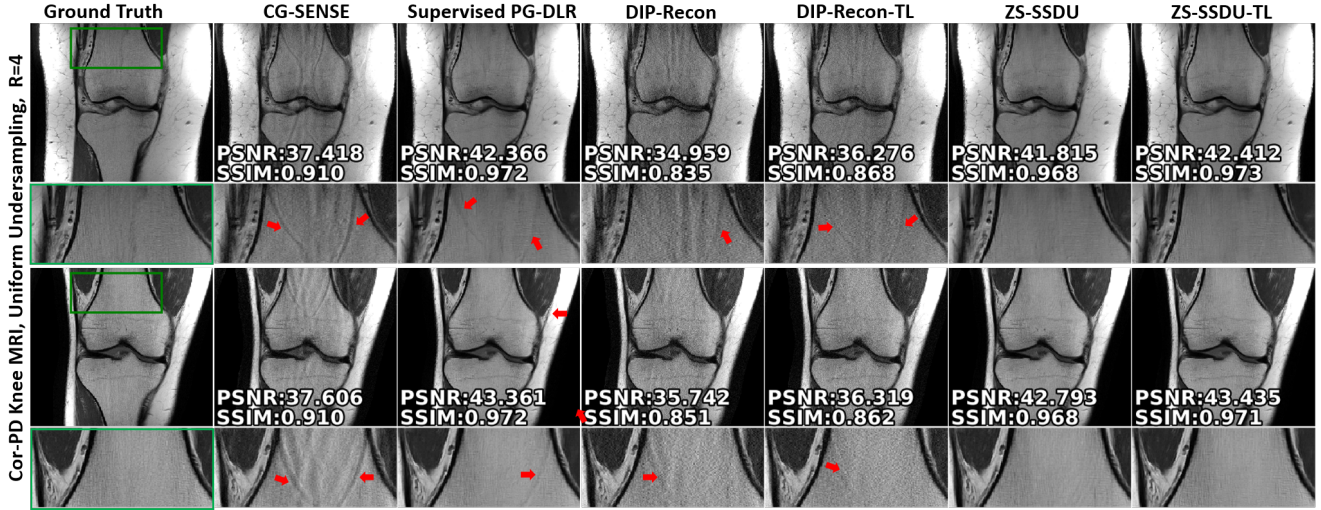


Figure S3. Representative reconstruction results from Cor-PD knee MRI at R = 4 with uniform undersampling, showing visible residual artifacts for supervised PG-DLR. CG-SENSE, DIP-Recon and DIP-Recon-TL suffer from aliasing artifacts and noise amplification. In these test slices, supervised PG-DLR also suffers from residual artifacts shown with red arrows, indicating generalizability issues that are not reflected in the quantitative metrics. On the other hand, ZS-SSDU and ZS-SSDU-TL achieve artifact-free and improved reconstruction quality, outperforming database-trained supervised PG-DLR in terms of artifact removal.

	Metrics	Supervised PG-DLR	DIP-Recon-TL	ZS-SSDU-TL
Figure 7: Banding Artifacts	SSIM	<b>0.873</b>	0.530	0.861
	PSNR	<b>36.365</b>	26.924	36.121
Figure 8a: In-Domain Transfer - Different Mask	SSIM	0.949	0.836	<b>0.951</b>
	PSNR	39.167	34.093	<b>40.088</b>
Figure 8b: In-Domain Transfer - Different Rates	SSIM	0.937	0.792	<b>0.940</b>
	PSNR	38.262	32.658	<b>38.301</b>
Figure 9a: Cross-Domain Transfer - Knee-Different Contrast	SSIM	0.931	0.859	<b>0.949</b>
	PSNR	37.566	34.855	<b>39.855</b>
Figure 9b: Cross-Domain Transfer - Brain-Different Contrast	SSIM	0.929	0.834	<b>0.950</b>
	PSNR	35.578	32.655	<b>38.767</b>
Figure 10a: Anatomy Change - Trained on Brain & Tested on Knee	SSIM	0.936	0.890	<b>0.957</b>
	PSNR	37.494	35.458	<b>40.407</b>
Figure 10b: Anatomy Change - Trained on Knee & Tested on Brain	SSIM	0.929	0.806	<b>0.936</b>
	PSNR	36.242	30.849	<b>37.134</b>

Table S1. Average PSNR and SSIM values on 30 test slices for the experiments associated with Figures 7-10 in the main text.